Conversion of Magnetic Energy to Plasma Kinetic Energy During Guide Field Magnetic Reconnection in the Laboratory

Sayak Bose,[1,*] William Fox,[1,2] Hantao Ji,[1,2] Jongsoo Yoo,[1] Aaron Goodman,[3] Andrew Alt,[2] and Masaaki Yamada[1]

[1] *Princeton Plasma Physics Laboratory, Princeton, New Jersey 08540, USA*
[2] *Department of Astrophysical Sciences, Princeton University, New Jersey 08540, USA*
[3] *Department of Mechanical and Aerospace Engineering, Princeton University, New Jersey 08540, USA*

We present laboratory measurements showing the two-dimensional (2D) structure of energy conversion during magnetic reconnection with a guide field over the electron and ion diffusion regions, resolving the separate energy deposition on electrons and ions. We find that the electrons are energized by the parallel electric field at two locations, at the X line and around the separatrices. On the other hand, the ions are energized ballistically by the perpendicular electric field in the vicinity of the high-density separatrices. An energy balance calculation by evaluating the terms of the Poynting theorem shows that 40% of the magnetic energy is converted to particle energy, 2/3 of which is transferred to ions and 1/3 to electrons. Further analysis suggests that the energy deposited on particles manifests mostly in the form of thermal kinetic energy in the diffusion regions.

Magnetic reconnection is a fundamental process in plasmas that leads to a change in the magnetic field topology accompanied by the conversion of magnetic energy to plasma kinetic energy [1]. Often during reconnection, there is a component of the magnetic field called the guide field (GF) perpendicular to the plane of the antiparallel components. GF reconnection is observed to energize electrons and ions in fusion plasmas [2, 3], basic physics experiments [4–6], the solar wind [7], solar flares [8], and the Earth's magnetosphere [9–13].

Multiple mechanisms of electron [14–16] and ion energization [17, 18] are proposed during GF reconnection. Satellite measurements of GF reconnection sites provide insight into kinetic-scale physics [9–13, 19]. Sparse measurements by a few satellites, however, have not been sufficient to quantify particle energization on a global scale due to the complex structures around the reconnection site. Comprehensive laboratory measurements of key parameters under well-defined, repeatable conditions are ideal for complementing simulations and satellite observation. However, early GF reconnection experiments were only performed in a regime where ions were unmagnetized over the system size, and the ion skin depth was much larger than the system size [20].

In this Letter, we present the first laboratory measurements of two-dimensional (2D) profiles of energy deposition on electrons and ions during GF reconnection in the regime where ions were sufficiently magnetized over the system size, and the ion skin depth was small enough for the electron and ion dynamics to be coupled. We significantly extend prior GF reconnection experiments [21, 22] by obtaining separate measurements of electron and ion flows, allowing determination of energy deposition onto each species. The energy deposition onto electrons is dominated by $\mathbf{E}_{\parallel}$, in two regions of the reconnection layer: around the X line and near the separatrices. The energy deposition on ions is dominated by $\mathbf{E}_{\perp}$ which is sufficiently strong to demagnetize and ballistically energize ions, in the vicinity of the high-density separatrices where electrons flow against the electric field. Furthermore, we determine how the energy is partitioned during GF reconnection, including enhancement of electron and ion kinetic energy in the form of thermal energy.

The experiments were conducted in the Magnetic Reconnection Experiment (MRX) [23, 24] (see Appendix for methodology) for a moderate GF of magnitude 122 G at the X line. The upstream reconnecting magnetic field at a distance of $1\rho_s$ from the X line is around 131 G, where $\rho_s = 3.9$ cm is the ion sound gyroradius calculated using electron temperature (T_e) and the total upstream magnetic field. Typical reconnection electric field ranges from 1 to 1.5 V/cm. The classical Spitzer resistivity accounts for approximately 9% of the reconnection electric field.

The features of the reconnection layer are shown in Fig. 1. Figure 1(a) displays representative magnetic

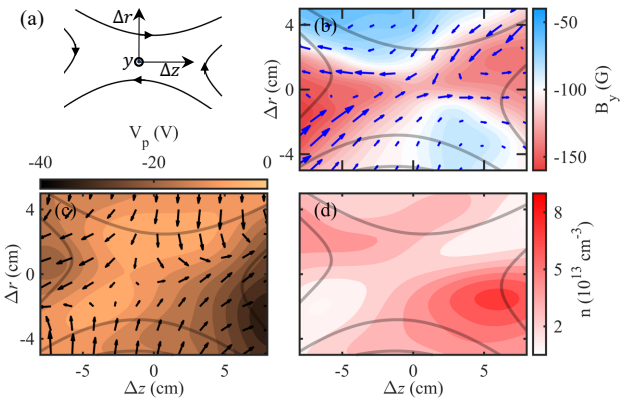

FIG. 1. (a) Representative reconnecting and reconnected magnetic field lines, and the coordinate system with respect to the X-point. The 2-D profiles of the (b) out of plane magnetic field, (c) plasma potential, and (d) density in the reconnection plane. The blue arrows in (b) represent the electron velocity vectors, while the black arrows in (c) represent the ion velocity vectors.

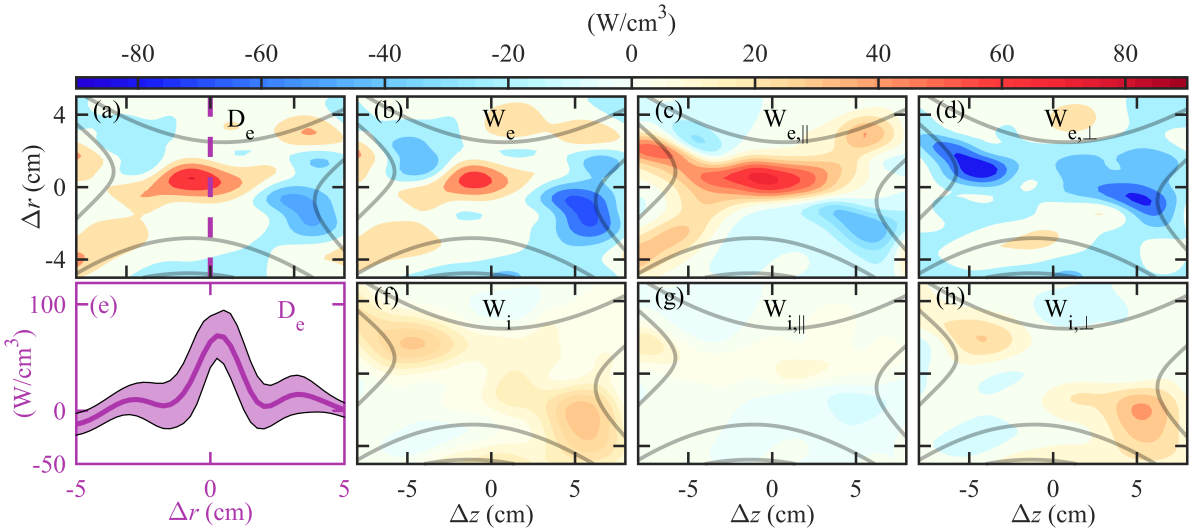

FIG. 2. 2-D profiles of scalar products that quantify power deposition on electrons and ions. (a) $D_e = \mathbf{J}\cdot\mathbf{E}'$, (b) $W_e = \mathbf{J}_e\cdot\mathbf{E}$, (c) $W_{e,\parallel} = J_{e,\parallel}E_\parallel$, (d) $W_{e,\perp} = \mathbf{J}_{e,\perp}\cdot\mathbf{E}_\perp$, (f) $W_i = \mathbf{J}_i\cdot\mathbf{E}$, (g) $W_{i,\parallel} = J_{i,\parallel}E_\parallel$, and (h) $W_{i,\perp} = \mathbf{J}_{i,\perp}\cdot\mathbf{E}_\perp$. The remaining plot in (e) is a 1-D cut of D_e to illustrate the representative 1-σ error bars.

field lines in the reconnection plane, i.e., the r-z plane. The 2D profile of the out-of-plane magnetic field (B_y) in Fig. 1(b) exhibits a quadrupolar structure, indicating the presence of two-fluid effects [25]. The plasma potential calculated using $V_\mathrm{p} = V_\mathrm{f} + 3.7T_e$ [26] also displays a quadrupolar structure [see Fig. 1(c)] [27]. Here V_p and V_f are the plasma potential and floating potential, respectively. The 2-D profile of density (n) reveals a pair of high density and low density regions in the vicinity of the separatrices [Fig. 1(d)] [22]. The n and V_p data exhibits a correlation; n is high at regions where V_p is more negative.

The arrows in Fig. 1(b) depict the flow of electrons in the reconnection region. The electron velocity is derived from the current profile using $\mathbf{v}_e = \mathbf{v}_i - \mathbf{J}/en$, where e is the quantum of electric charge, $\mathbf{J}$ is the surface current density, and $\mathbf{v}_e$ and $\mathbf{v}_i$ are the electron and ion velocity, respectively. The electron velocity vectors show that electrons enter the reconnection layer along a pair of low density separatrices and are ejected out through the high density side of the reconnection layer. The electron inflow velocity is greater than the outflow velocity. The ion flow velocity vectors in the reconnection plane are shown in Fig. 1c. A comparison of the electron and ion velocity vectors unambiguously demonstrates that the trajectories of the electron and ion fluids are significantly different in the reconnection layer.

The conversion of the magnetic energy to the plasma kinetic energy is mediated by an electric field which is given by Ohm's law (the electron momentum equation),

$$\mathbf{E} + \mathbf{v}_e \times \mathbf{B} = -\frac{m_e}{e}\frac{d\mathbf{v}_e}{dt} - \frac{\nabla\cdot\overleftrightarrow{P}_e}{en} + \eta_\parallel\mathbf{J}_\parallel + \eta_\perp\mathbf{J}_\perp, \quad (1)$$

where m_e is the mass of the electron, $\overleftrightarrow{P}_e$ is the electron pressure tensor, and η is the Spitzer resistivity. The power deposition per unit volume on particles due to the nonideal terms of Ohm's law on the rhs of Eq. 1 is given by $D_e = \mathbf{J}\cdot\mathbf{E}'$, where $\mathbf{E}' = \mathbf{E} + \mathbf{v}_e\times\mathbf{B}$, the electric field due to nonideal terms [28]. A positive value of D_e indicates the region of magnetic energy deposition where the frozen-in condition of the electrons is violated, i.e. $\mathbf{E}' = \mathbf{E} + \mathbf{v}_e\times\mathbf{B} \neq 0$. However, D_e does not differentiate between energy deposition onto electrons and ions. While the electrons can only be energized by the nonideal terms because $\mathbf{v}_e\cdot(\mathbf{v}_e\times\mathbf{B}) = 0$, the ions may gain energy from the non-ideal terms as well as from the $-(\mathbf{v}_e\times\mathbf{B})$ term. Therefore, to quantify the rate of work done on electrons and ions we calculate $W_e = \mathbf{J}_e\cdot\mathbf{E}$ $(= \mathbf{J}_e\cdot\mathbf{E}')$ and $W_i = \mathbf{J}_i\cdot\mathbf{E}$, respectively.

The 2-D profile of D_e depicted in Fig. 2(a) shows that the energy conversion from the magnetic field to the plasma kinetic energy is mediated by $\mathbf{E}'$ at multiple locations in the reconnection plane. The rate of energy deposition per unit volume is most intense near the X line where D_e is as high as 80 W/cm^3. D_e is also positive in the electron inflow region near the separatrices revealing regions of particle energization away from the X line. However, in the region with a strong electron outflow, the electrons flow against $\mathbf{E}'$. The representative 1-σ error bars are shown in Fig. 2(e) which depicts a 1D cut of D_e across the X line.

A comparison of the 2D profiles of D_e [Fig. 2(a)], W_e [Fig. 2(b)], and W_i [Fig. 2(f)] shows a remarkable similarity between D_e and W_e. This resemblance suggests that the nonideal terms of Ohm's law channel most of the magnetic energy to electrons.

Since the dynamics of charged particles parallel and perpendicular to the magnetic field are different, it is

instructive to calculate the energy deposition driven by $\mathbf{E}_\parallel$ and $\mathbf{E}_\perp$. $W_{e,\parallel}$, $W_{e,\perp}$, $W_{i,\parallel}$, and $W_{i,\perp}$ are depicted in Figs. 2(c), 2(d), 2(g), and 2(h), respectively. $W_{e,\parallel}$ is computed using $J_{e,\parallel} = \mathbf{J}_e \cdot \hat{\mathbf{b}}$ and $E_\parallel = \mathbf{E} \cdot \hat{\mathbf{b}}$, where $\hat{\mathbf{b}}$ is a unit vector along the magnetic field. $W_{e,\perp}$ is determined from the dot product of $\mathbf{J}_{e,\perp} = \mathbf{J}_e - \mathbf{J}_{e,\parallel}$ and $\mathbf{E}_\perp = \mathbf{E} - \mathbf{E}_\parallel$. Similarly, we have worked out $W_{i,\parallel}$ and $W_{i,\perp}$.

The electrons are energized by $E_\parallel$ in two regions of the reconnection layer: most intensely near the X line and additionally in the vicinity of the separatrices over the ion scale, as shown in Fig. 2(c). Previously, Fox *et al.* [22] have shown that $\mathbf{E}_\parallel$ in the ion diffusion region is approximately supported by the pressure gradient term of Ohm's law, i.e., $\mathbf{E}_\parallel \approx -\nabla_\parallel P_e/en$. Extending on that finding, we observe $J_{e,\parallel}E_\parallel \approx \mathbf{v}_{e,\parallel}\cdot\nabla_\parallel P_e$. For example, at $\Delta r = -2.25$ cm and $\Delta z = 5.75$ cm, $J_{e,\parallel}E_\parallel$ and $\mathbf{v}_{e,\parallel}\cdot\nabla_\parallel P_e$ are 31 W/cm^3 and 27 W/cm^3, respectively. The positive and negative values of $J_{e,\parallel}E_\parallel$ in the ion diffusion region indicate compression and decompression of the electron fluid. Similarly, the negative values of $\mathbf{J}_{e,\perp}\cdot\mathbf{E}_\perp$ in the electron outflow region in Fig. 2(d) suggest decompression.

The structure of $W_{e,\parallel}$ in Fig. 2(c) is rather interesting. The electrons approaching the reconnection layer along $\mathbf{B}$ are continuously under the influence of $\mathbf{E}_\parallel$ until the X line. In natural systems, where the electron mean free path is significantly large compared to laboratory experiments, an "acceleration-channel"-like feature where electrons are continuously under the influence of the driver term, $\mathbf{E}_\parallel$, over large distances may explain the observation of high energy electrons associated with GF reconnection [29, 30].

The 2D profile of W_i depicted in Fig. 2(f) shows that the regions of intense ion energization are well-structured and located in the electron outflow region, and are dominated by $\mathbf{E}_\perp$ [Fig. 2(h)] over $E_\parallel$ [Fig. 2(g)]. The $E_\perp$ varies from 3 to 6 V/cm in the region of intense energization. Interestingly, the 2D profiles of W_e [Fig. 2(b)] and W_i [Fig. 2(f)] show that the regions of electron and ion energization are rather complementary. The electrons are energized near the low-density separatrices and at the X line, while the ions gain energy in the vicinity of the high-density separatrices where the electrons work against the electric field. This suggest that electrons may transfer their energy to ions via the electric field.

$\mathbf{E}_\perp$ can energize the ions in two ways: the ions can be energized ballistically when ions are unmagnetized, or $\mathbf{E}_\perp$ can drive ion polarization drift that adiabatically increases the ion velocity to reach the $\mathbf{E}\times\mathbf{B}$ outflow velocity. To distinguish between these two processes we compare the relevant length and time scales with the estimated ion gyroradius (ρ_i) and gyroperiod (τ_i), respectively. The length scale of the magnetic field $L_B = |B/\nabla B|$ in the region of ion energization at $\Delta z = -5$ cm and $\Delta r = 1$ cm is 6 cm which is comparable to $\rho_i = 4$ cm. We used $T_i = 6.5$ eV measured by ion Doppler spectroscopy and the local value of B to estimate ρ_i. The width of the ion energization region in both the upper left and lower right of Fig. 2(f) is ≈ 5 cm, which is comparable to ρ_i. The ion transit time, τ, through the region of intense ion energization in the upper left of Fig. 2(f) is ≈ 7 μs, which is almost a third of $\tau_i \approx 20$ μs. Similarly in the lower right $\tau < \tau_i$. Thus, we conclude that strong $\mathbf{E}_\perp$ energize the demagnetized ions ballistically.

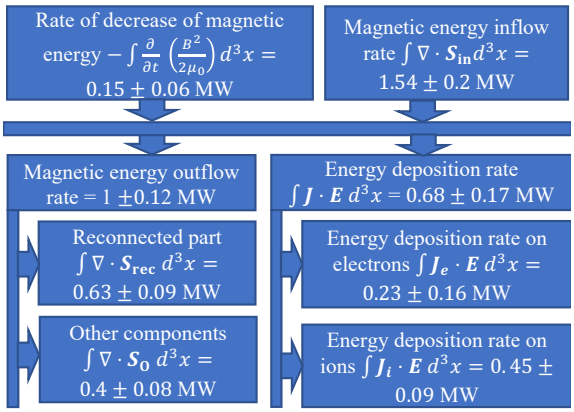

FIG. 3. Energy partition during GF reconnection during quasi-steady period. The time variation of the energy partition quantities are within the error bars. The integration box covers an area of $4.1 \times 4.4\rho_s$.

The energy partition among electrons, ions, and other channels during GF reconnection is analyzed by calculating the terms of the Poynting theorem,

$$-\int \frac{\partial}{\partial t}\left(\frac{B^2}{2\mu_0}\right) d^3x = \int \nabla\cdot(\mathbf{S_{in}} + \mathbf{S_{rec}} + \mathbf{S_o})\, d^3x + \int (\mathbf{J}_e\cdot\mathbf{E} + \mathbf{J}_i\cdot\mathbf{E})\, d^3x, \quad (2)$$

where integration is carried out over reconnection volume assuming toroidal symmetry. Here, $\mathbf{S_{in}} = (E_y B_z/\mu_0)\,\hat{\mathbf{r}}$ is the incoming Poynting flux associated with the reconnecting magnetic field and the reconnection electric field, and the outgoing Poynting flux is divided into $\mathbf{S_{rec}}$ and $\mathbf{S_o}$. The $\mathbf{S_{rec}} = -(E_y B_r/\mu_0)\,\hat{\mathbf{z}}$ is associated with the reconnected magnetic field and the reconnection electric field. While $\mathbf{S_o} = (E_r B_y/\mu_0)\,\hat{\mathbf{z}} - (E_z B_y/\mu_0)\,\hat{\mathbf{r}}$, is associated with the Hall magnetic field superimposed on the guide field, and the electrostatic electric fields.

The results of the Poynting theorem analysis are shown in Fig. 3. The reconnecting magnetic field delivers 1.54 MW of power to the reconnection layer. There is a slight decrease of magnetic field during reconnection resulting in a reduction of 0.15 MW in magnetic power. 1 MW of magnetic power flows out of the reconnection layer. The bulk of the outflow is due to the Poynting vector associated with the reconnected magnetic field, which

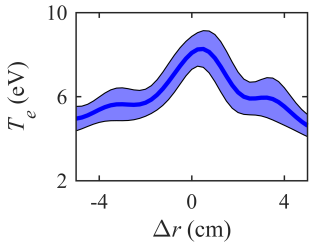

FIG. 4. Radial variation of T_e at $\Delta z = 0$ cm.

is 0.63 MW, while the rest is accounted for by the outgoing toroidal magnetic field. Around 40% of the magnetic energy is deposited on the particles, 1/3 of which goes to electrons and 2/3 to ions.

The energy deposited on electrons and ions may manifest in the form of thermal energy, causing an increase in temperature, or causing acceleration resulting in a gain of flow energy. The electron temperature measurement showed an enhancement in T_e in the vicinity of the X line where a significant amount of energy is deposited on electrons [see Fig. 2(b) for $\mathbf{J_e} \cdot \mathbf{E}$]. Figure 4 shows the radial variation of T_e. We observe that T_e increases from 5 eV at 5 cm away from the X-line to 8 eV at the X line taken at $\Delta z = 0$. This increase in T_e is more than 50% and beyond the measurement uncertainty. The change in the electron thermal energy per unit time estimated using $\Delta W_{\mathrm{H,e}} \approx \int \nabla \cdot \left(\frac{5}{2} n T_e \mathbf{v_e}\right) d^3x$ is ~ 0.1 MW. This is smaller but on the same order as the magnetic energy deposition rate on electrons calculated by $\int \mathbf{J_e} \cdot \mathbf{E}\, d^3x$. The change in the electron flow energy per unit time is negligibly small [$\Delta W_{\mathrm{flow},e} \approx \int \nabla \cdot \left(\frac{1}{2} m_e n v_e^2 \mathbf{v}_e\right) d^3x < 7$ W] because of the low mass of electrons. Therefore, the rate of energy deposited on electrons not observed in $\Delta W_{\mathrm{H,e}}$ is expected to be accounted for by loss mechanisms like the thermal conductivity parallel to the magnetic field [31–34]. This is expected to be large as it scales as $T_e^{7/2}$ but is difficult to estimate due to its sensitivity to the T_e gradient.

The T_i measurements suggest an increase in ion thermal energy during GF reconnection. In the right half of the reconnection plane near the exhaust, T_i is 9 eV, while in the left half exhaust T_i is 6.5 eV. T_i could not be measured in the upstream region due to low emission (due to low T_e) there. Nevertheless, previous MRX experiments [31] have shown that $T_i \approx T_e$ in the upstream region. Using this assumption, we estimate the increase in the thermal energy of the ions per unit time to be ~ 0.2 MW. This is within a factor of $2-3$ of $\int \mathbf{J_i} \cdot \mathbf{E}\, d^3x$. However, the change in the ion flow energy per unit time is very small [$\Delta W_{\mathrm{flow},i} \approx \int \nabla \cdot \left(\frac{1}{2} m_i n v_i^2 \mathbf{v}_i\right) d^3x < 0.02$ MW] as the ion flow measurements are confined to the ion diffusion region limiting the formation of an Alfvénic outflow.

The gap between $\int \mathbf{J_i} \cdot \mathbf{E}\, d^3x$ and the increase in ion thermal energy per unit time is expected to be accounted for by loss channels. A well-known energy loss mechanism for ions in MRX is the charge exchange collision with neutrals [33]. The measured neutral temperature of 3.3 eV during GF reconnection in the downstream region supports ion energy loss via the charge exchange mechanism. Assuming a uniform neutral density in the reconnection layer we estimate that the maximum ion energy loss per unit time to neutrals to be ~ 0.15 MW. In addition, ion energy loss is also expected to occur due to thermal conduction to the exhaust [31].

The above analysis showed that similar energy partition occurs between electrons and ions during GF reconnection as in antiparallel reconnection [32]. This is interesting as there are significant differences between GF and antiparallel reconnection beyond the obvious presence of GF. The 2D profile of V_{p} and n exhibits a tilted quadrupolar structure in GF reconnection which is different from antiparallel reconnection. The electrons are energized by $\mathbf{E}_{\parallel}$ and the electron inflow velocity is greater than the outflow velocity in GF reconnection, while in the antiparallel case, $\mathbf{E}_{\perp}$ energizes the electrons, and the electron outflow velocity is greater than the inflow velocity [32, 33]. The regions of ion energization are structured in GF reconnection. The ions gain energy in the vicinity of high density separatrices with spatial extent of around ρ_i, in contrast to during the antiparallel reconnection where the ions gain energy over a wide region in the exhaust [35]. Our experiment provides noteworthy constraints by identifying factors that may not appreciably affect the energy partition between the electrons and ions in the reconnection layer.

In summary, to study the conversion of the magnetic energy to the plasma kinetic energy during GF reconnection, we have compared 2D profiles of key energy deposition scalar products, $\mathbf{J} \cdot \mathbf{E}'$, $\mathbf{J}_e \cdot \mathbf{E}$, $J_{e,\parallel} E_{\parallel}$, $\mathbf{J}_{e,\perp} \cdot \mathbf{E}_{\perp}$, $\mathbf{J}_i \cdot \mathbf{E}$, $J_{i,\parallel} E_{\parallel}$, and $\mathbf{J}_{i,\perp} \cdot \mathbf{E}_{\perp}$. The electrons entering the reconnection layer along $\mathbf{B}$ are energized by $\mathbf{E}_{\parallel}$ in the vicinity of the low-density sepratrices. $\mathbf{E}_{\parallel}$ energizes electrons all the way until the X line forming an "acceleration-channel"-like feature. The electron energization is most intense at the X line. The outgoing electrons flow against the electric field near the high density separatrices. The ions are energized ballistically by $\mathbf{E}_{\perp}$ in the vicinity of the high density separatrices in the outflow region. The energy conversion results are complemented by 2D measurements of physical quantities that characterize the reconnection layer and provide references to compare our results to relevant regions in space observations, other laboratory experiments, and simulations.

The energy balance analysis by evaluating the terms of the Poynting theorem shows that 40% of the magnetic energy is deposited on particles with a 1:2 ratio to electrons and ions. Additional measurements showed that the energy deposited on electrons manifests as thermal energy, part of which increases T_e while the rest is most probably transported to the exhaust by heat conduction. The energy deposited on ions enhances T_i with a

dominant loss due to charge exchange collisions and also loss due to thermal conduction is expected. Future work would be to experimentally evaluate important terms of the electron and ion energy transport equations [33, 36] so that their temperature increases can be understood in the context of finite energy transport and loss channels in the reconnection layer.

The authors would like to thank Dr. Jon Jara-Almonte for stimulating discussions. The authors thank Mr. Peter Sloboda for his help in making the drive coils. This work was supported Max-Planck Princeton Center for Plasma Physics, funded by US Department of Energy Contract No. DE- AC0209CH11466, and NASA under Agreements No. 80HQTR21T0053 and 80HQTR21T0060.

Data availability statement: Data underlying the results presented in this Letter will be made available via Princeton University's data repository upon publication.

Appendix on methodology: The experiments are conducted in the Magnetic Reconnection eXperiment (MRX) [23, 24]. A schematic of the experiment is shown in Fig. 5. The flux cores house the toroidal field (TF) and the poloidal field (PF) coils. The PF coils are used to produce antiparallel magnetic fields in the poloidal (r-z) plane of MRX. The toroidal GF, $-B_y\hat{y}$, is produced by passing a current through an axial conductor. A time-varying current through the TF coils produces an inductive electric field that breaks down the gas to produce plasma. Reconnection is driven by inducing the radial inflow and axial outflow of the plasma from the reconnection layer by increasing the current in the upstream drive coils and ramping down the current in the PF coils. The reconnection is quasisteady in this mode of operation where the time scale of variation of the plasma current is greater than the ion-transit time. The data reported in this Letter were acquired during the quasisteady period as in previous experiments on MRX [21, 22, 31–33, 35].

The experiments are carried out using Helium gas with a fill pressure of 4×10^{-3} Torr. Multiple triaxial B-dot probe arrays covering the reconnection layer are used for the magnetic-field measurements. The current density is calculated from the magnetic field using Ampère's law, $\mathbf{J} = \nabla \times \mathbf{B}/\mu_0$, where μ_0 is the permeability of free space. The inductive reconnection electric field, E_y, is determined from the rate of change of poloidal magnetic flux using Faraday's law assuming toroidal symmetry.

The electron density (n), temperature (T_e), and floating potential (V_f) are measured using a Langmuir probe [34]. The ion velocity, $\mathbf{v}_i$, is measured using Mach probes, which were calibrated using the ion velocity measured by the ion Doppler spectroscopy probe [34, 35]. The electric probes are scanned between shots to sample the r-z plane. A total of 1,700 shots are scrutinized to assemble a refined dataset, based on consistency in magnetic-field structure and reference Langmuir probe data. A minor shot-to-shot variation in the X line location is corrected by using the relative position of the probes with respect to the X line.

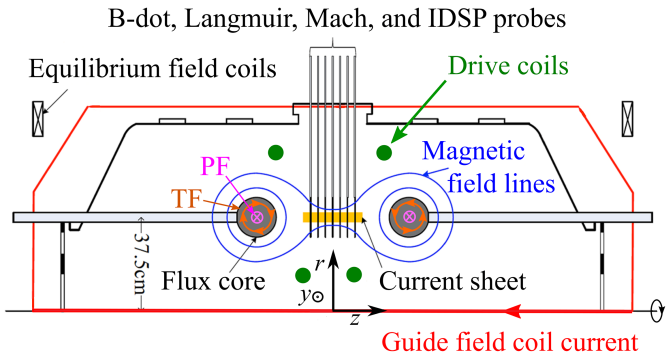

FIG. 5. Schematic of MRX showing the adopted coordinate system (r, y, z), the coils used to induce and drive reconnection, and different diagnostics used for making measurements. See the text and Refs. [22–24] for detailed description.

Gaussian process regression (GPR) [37], a class of machine learning algorithms, is utilized to construct 2D data planes from the discrete datasets of electric probes. GPR makes predictions using the trends in the dataset without assuming any specific functional form. We train a GPR model with a radial basis function kernel for each directly measured quantity using the discrete dataset [38]. The mean profiles and variances are extracted from the posterior of the trained GPR model. The error propagation analysis for composite quantities (for example, $\mathbf{J}_i = en\mathbf{v}_i$) is done using a Monte Carlo method. Samples are drawn randomly from the profiles of input quantities (n and $\mathbf{v}_i$) according to their respective uncertainty estimates. These samples are used to construct an ensemble of possible realization of outputs (a set of $\mathbf{J}_i$) from which variances are calculated [39]. Refer to the Supplemental Material [40] for more details on application of GPR, and error analysis.

* sbose@princeton.edu

[1] D. Biskamp, *Magnetic Reconnection in Plasmas*, Cambridge Monographs on Plasma Physics (Cambridge University Press, 2000).
[2] Y. Ono, H. Tanabe, T. Yamada, K. Gi, T. Watanabe, T. Ii, M. Gryaznevich, R. Scannell, N. Conway, B. Crowley, *et al.*, Physics of Plasmas **22**, 055708 (2015).
[3] H. Tanabe, T. Yamada, T. Watanabe, K. Gi, M. Inomoto, R. Imazawa, M. Gryaznevich, R. Scannell, N. Conway, C. Michael, *et al.*, Nuclear Fusion **57**, 056037 (2017).
[4] A. Stark, W. Fox, J. Egedal, O. Grulke, and T. Klinger, Physical Review Letters **95**, 235005 (2005).
[5] R. Stenzel, W. Gekelman, and N. Wild, Journal of Geophysical Research: Space Physics **87**, 111 (1982).
[6] T. Tharp, M. Yamada, H. Ji, E. Lawrence, S. Dorfman, C. Myers, and J. Yoo, Physical Review Letters **109**, 165002 (2012).

[7] T. Phan, S. Bale, J. Eastwood, B. Lavraud, J. Drake, M. Oieroset, M. Shay, M. Pulupa, M. Stevens, R. MacDowall, *et al.*, The Astrophysical Journal Supplement Series **246**, 34 (2020).

[8] B. Chen, C. Shen, D. E. Gary, K. K. Reeves, G. D. Fleishman, S. Yu, F. Guo, S. Krucker, J. Lin, G. M. Nita, *et al.*, Nature Astronomy **4**, 1140 (2020).

[9] R. Ergun, K. Goodrich, F. Wilder, J. Holmes, J. Stawarz, S. Eriksson, A. Sturner, D. Malaspina, M. Usanova, R. Torbert, *et al.*, Physical Review Letters **116**, 235102 (2016).

[10] M. Øieroset, T. Phan, C. Haggerty, M. A. Shay, J. P. Eastwood, D. J. Gershman, J. F. Drake, M. Fujimoto, R. Ergun, F. Mozer, *et al.*, Geophysical Research Letters **43**, 5536 (2016).

[11] F. Wilder, R. Ergun, S. Eriksson, T. Phan, J. Burch, N. Ahmadi, K. Goodrich, D. Newman, K. Trattner, R. Torbert, *et al.*, Physical Review Letters **118**, 265101 (2017).

[12] Z. Li and M. Zhang, The Astrophysical Journal **888**, 5 (2019).

[13] S. Eriksson, F. Wilder, R. Ergun, S. Schwartz, P. Cassak, J. Burch, L.-J. Chen, R. Torbert, T. Phan, B. Lavraud, *et al.*, Physical Review Letters **117**, 015001 (2016).

[14] F. Pucci, S. Usami, H. Ji, X. Guo, R. Horiuchi, S. Okamura, W. Fox, J. Jara-Almonte, M. Yamada, and J. Yoo, Physics of Plasmas **25**, 122111 (2018).

[15] X. Guo, R. Horiuchi, C. Cheng, Y. Kaminou, and Y. Ono, Physics of Plasmas **24**, 032901 (2017).

[16] C. Huang, Q. Lu, and S. Wang, Physics of Plasmas **17**, 072306 (2010).

[17] R. G. Kleva, J. Drake, and F. Waelbroeck, Physics of Plasmas **2**, 23 (1995).

[18] K. Knizhnik, M. Swisdak, and J. F. Drake, The Astrophysical Journal Letters **743**, L35 (2011).

[19] K. Genestreti, J. Burch, P. Cassak, R. Torbert, R. Ergun, A. Varsani, T. Phan, B. Giles, C. Russell, S. Wang, *et al.*, Journal of Geophysical Research: Space Physics **122**, 11 (2017).

[20] N. Wild, W. Gekelman, and R. Stenzel, Physical Review Letters **46**, 339 (1981).

[21] W. Fox, F. D. Wilder, S. Eriksson, J. Jara-Almonte, F. Pucci, J. Yoo, H. Ji, M. Yamada, R. Ergun, M. Oieroset, *et al.*, Geophysical Research Letters **45**, 12 (2018).

[22] W. Fox, F. Sciortino, A. v. Stechow, J. Jara-Almonte, J. Yoo, H. Ji, and M. Yamada, Physical Review Letters **118**, 125002 (2017).

[23] M. Yamada, H. Ji, S. Hsu, T. Carter, R. Kulsrud, N. Bretz, F. Jobes, Y. Ono, and F. Perkins, Physics of Plasmas **4**, 1936 (1997).

[24] H. Ji, Y. Ren, M. Yamada, S. Dorfman, W. Daughton, and S. Gerhardt, Geophysical Research Letters **35** (2008).

[25] D. A. Uzdensky and R. M. Kulsrud, Physics of Plasmas **13**, 062305 (2006).

[26] H. Ji, H. Toyama, K. Yamagishi, S. Shinohara, A. Fujisawa, and K. Miyamoto, Review of Scientific Instruments **62**, 2326 (1991).

[27] J. Egedal, A. Fasoli, and J. Nazemi, Physical Review Letters **90**, 135003 (2003).

[28] S. Zenitani, M. Hesse, A. Klimas, and M. Kuznetsova, Phys. Rev. Lett. **106**, 195003 (2011).

[29] G. D. Holman, Advances in Space Research **35**, 1669 (2005).

[30] A. Abdo, M. Ackermann, M. Ajello, A. Allafort, L. Baldini, J. Ballet, G. Barbiellini, D. Bastieri, K. Bechtol, R. Bellazzini, *et al.*, Science **331**, 739 (2011).

[31] J. Yoo, M. Yamada, H. Ji, J. Jara-Almonte, and C. E. Myers, Physics of Plasmas **21**, 055706 (2014).

[32] M. Yamada, J. Yoo, J. Jara-Almonte, H. Ji, R. M. Kulsrud, and C. E. Myers, Nature communications **5**, 1 (2014).

[33] M. Yamada, J. Yoo, J. Jara-Almonte, W. Daughton, H. Ji, R. M. Kulsrud, and C. E. Myers, Physics of Plasmas **22**, 056501 (2015).

[34] J. Yoo, *Experimental studies of particle acceleration and heating during magnetic reconnection*, Ph.D. thesis, Princeton University (2013).

[35] J. Yoo, M. Yamada, H. Ji, and C. E. Myers, Physical Review Letters **110**, 215007 (2013).

[36] S. I. Braginskii, Reviews of Plasma Physics **1**, 205 (1965).

[37] C. E. Rasmussen, *Gaussian processes for machine learning /*, Adaptive Computation and Machine Learning series (MIT Press,, Cambridge, Mass. :, 2005-01-01).

[38] F. Pedregosa, G. Varoquaux, A. Gramfort, V. Michel, B. Thirion, O. Grisel, M. Blondel, P. Prettenhofer, R. Weiss, V. Dubourg, J. Vanderplas, A. Passos, D. Cournapeau, M. Brucher, M. Perrot, and E. Duchesnay, Journal of Machine Learning Research **12**, 2825 (2011).

[39] M. Chilenski, M. Greenwald, Y. Marzouk, N. Howard, A. White, J. Rice, and J. Walk, Nuclear Fusion **55**, 023012 (2015).

[40] See supplemental material at [url] for more information on the application of Gaussian Process Regression for reconstruction of 2-D data planes from discrete measurements, and error propagation. The supplemental material also includes Refs. [41–45],.

[41] A. Mathews and J. W. Hughes, IEEE Transactions on Plasma Science **49**, 3841 (2021).

[42] J. Wang, arXiv preprint arXiv:2009.10862 (2020).

[43] Q.-H. Zhang and Y.-Q. Ni, IEEE Transactions on Signal Processing **68**, 3450 (2020).

[44] M. Chilenski, M. Greenwald, A. Hubbard, J. Hughes, J. Lee, Y. Marzouk, J. Rice, and A. White, Nuclear Fusion **57**, 126013 (2017).

[45] Gaussian processes, https://scikit-learn.org/stable/modules/gaussian_process.html, [Online; accessed 5-July-2023].

Supplemental Material: Implementation of Gaussian Process Regression to Reconstruct 2D Data Planes from Discrete Measurements and Propagate Error Bars

Sayak Bose,[1,*] William Fox,[1,2] Hantao Ji,[1,2] Jongsoo Yoo,[1] Aaron Goodman,[3] Andrew Alt,[2] and Masaaki Yamada[1]

[1] *Princeton Plasma Physics Laboratory, Princeton, New Jersey 08540, USA*
[2] *Department of Astrophysical Sciences, Princeton University, New Jersey 08540, USA*
[3] *Department of Mechanical and Aerospace Engineering, Princeton University, New Jersey 08540, USA*

I. INTRODUCTION

Gaussian process regression (GPR) is a class of supervised machine learning algorithms that can be used to construct data profiles from discrete observations, predict uncertainty in the reconstructed profiles in a statistically rigorous manner and provide the framework for error propagation in the calculation of quantities derived from the data profiles [1–3]. Compared to traditional parametric fitting methods, GPR is particularly useful in data reconstruction from discrete observations where the plasma is non-uniform, and the function describing the non-uniform profile is not known beforehand. To elaborate, traditional fitting methods assume a parametric form of a function before fitting that function to a discrete set of observations. A limitation of the traditional method is that more than one function can fit a discrete set of observations, and often plasma physics theories don't predict which functional form is preferred. GPR is a Bayesian non-parametric regression technique that predicts a probability distribution over possible functions that fit a set of discrete data points. The mean of the probability distribution gives the most probable characterization of the data, i.e., the mean function (mean profile), while the standard deviation obtained from variance indicates the uncertainty in the prediction. Thus, GPR recognizes that there is an uncertainty in the function describing the data profiles, which is not acknowledged in traditional fitting methods where a functional form is assumed for fitting [1, 4].

GPR models assume that the measured discrete data points are part of a multivariate normal distribution, i.e., the data points measured at a particular spatial location satisfy a univariate normal distribution, while the data points at neighboring locations are correlated. The correlation between neighboring data points enables GPR to make predictions at locations where measurement does not exist. A covariance kernel like the Radial Basis Function (RBF) is used to incorporate the correlation between data points in the GPR model.

GPR models are classified as homoscedastic and heteroscedastic models depending on how the variability in the observation is modeled [5]. In the context of pulsed experiments like MRX[6], the shot-to-shot variation cause observation variability. In a homoscedastic GPR model, the variance in the observation is assumed to be constant throughout the input space. An example will be a set of observations where the spread of the data points about the mean is the same at each measurement location. In the heteroscedastic model, the variance in the observation can change depending on the location in the input space. Heteroscedastic models are more relevant for experiments where the error bars can differ at different measurement locations. Heteroscedastic GPR uses two $\mathcal{GP}$s (Gaussian Processes), one for modeling the mean function and the other for modeling the input space-dependent error bars. A combination of the two $\mathcal{GP}$s give a posterior distribution over the mean function and input dependent error bars [5]. The mathematical basis for GPR and its application are well described in Refs [1, 2, 4, 5].

Recently, GPR has been used to reconstruct 1-D density and electron temperature profiles of a Tokamak (fusion device) [7]. Typically for analysis of Tokamak data, discrete measurements made at multiple spatial locations simultaneously in a single shot are used to reconstruct the 1-D profiles [7]. However, in MRX, data points from a large number of shots are assembled for the reconstruction of 2D profiles. The data variability due to shot-to-shot variation in MRX needs to be accounted for during profile reconstruction, gradient calculation, and uncertainty prediction. We describe the application of GPR for data analysis that considers the nuances of MRX data due to shot-to-shot variation.

II. APPLICATION OF GPR FOR ANALYZING MRX DATA

GPR was employed to construct 2D planes from the discete datsets of electric probes like Langmuir and Mach probes. We demonstrate the implementation of GPR by using the density and potential data of MRX as examples. The density and potential were measured using Langmuir probes [8]. The Langmuir probes were used to make single point measurements in each shot. The probes were moved between shots to obtain discrete data points covering the r-z plane of MRX. Discrete data points from a large number of shots were assimilated to form a dataset for application of GPR. An inspection of the raw data showed that the spread of the discrete data points about the mean differs at different spatial locations. Furthermore, simultaneous measurements at multiple locations showed that the change in the measured values due to

* sbose@princeton.edu

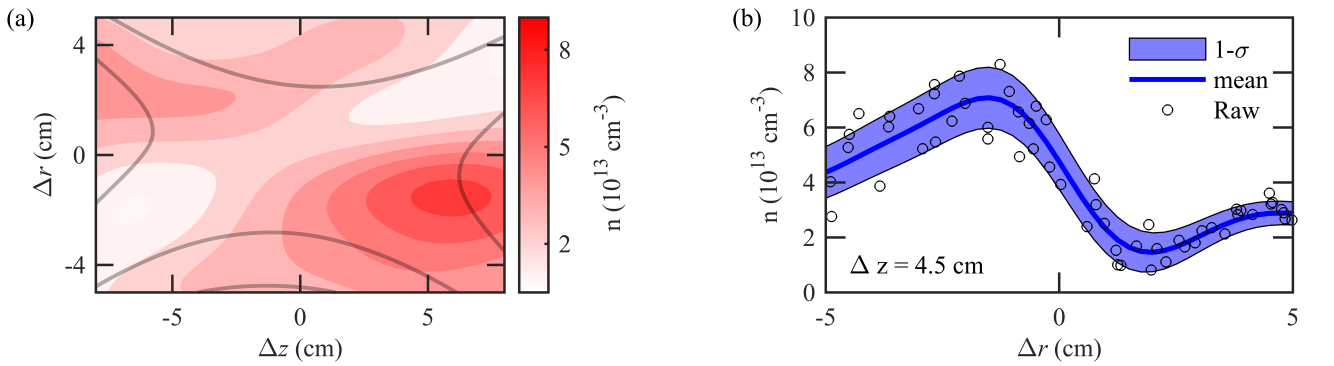

FIG. 1. (a) Two-dimensional mean profile of the electron density extracted from the posterior of a GPR model trained using the discrete raw data. The grey lines are representative magnetic field lines in the r-z plane for reference. (b) A 1-D plot showing the mean and standard deviation extracted from the posterior of the trained GPR model along with the raw data. The dark blue line is the mean density at $\Delta z = 4.5$ cm. The blue band gives the 1-σ uncertainty in the predicted mean profile from the trained GPR model, where σ is the standard deviation. The black circular dots are raw data points lying between $\Delta z = 4$ to 4.5 cm. Note that the 1-σ error bar follows the local spread in the data points. The error bar is thicker at $\Delta r \sim -2.5$ cm where the spread in the raw data is more, while the error bar is smaller at $\Delta r \sim 4.5$ cm where the spread in the raw data is less.

shot-to-shot variation is spatially correlated. To preserve these raw data features in our analysis, we adopted the heteroscedastic GPR model of Zhang and Ni [5]. The model implemented for data reconstruction can be written as

$$y(\mathbf{x}) = f(\mathbf{x}) + \mathcal{GP}\left(0, g(\mathbf{x})\,\rho(\mathbf{x},\mathbf{x}')\,g(\mathbf{x}')\right), \qquad (1)$$

where $y(\mathbf{x})$ is a sample from the posterior of the trained model, $f(\mathbf{x})$ is the mean function, g^2 is a measure of the variance, and ρ is the correlation function that incorporates the spatial correlation between the change in the measured values at neighboring locations due to shot-to-shot variation. The formulation of Zhang and Ni [5] is used to estimate $f(\mathbf{x})$ and g from two $\mathcal{GP}$s employing RBF Kernels. An RBF kernel with a length scale l of 1.5 cm is used to specify ρ. Refer to subsection II B for the role of length scale of ρ in the GPR model. For the functional form of the RBF kernel, also known as the squared exponential kernel, refer to Rasmussen [1].

Henceforth for brevity, the heteroscedastic GPR model used for reconstructing MRX data profiles will be referred to as the GPR model. The codes for the model were written using the freely available Python packages scikit-learn [9] and NumPy. For introductory examples on how $\mathcal{GP}$s are trained refer to the help files of scikit-learn [10].

A. Reconstruction of 2D data profiles and calculation of uncertainty in the predicted profile

We have used the density data to demonstrate the construction of 2D data profile using GPR. As mentioned before, a Langmuir probe was used to measure density. The Langmuir probe was used to make a single-point measurement in each shot. A large number of shots were taken where the probe was moved in-between shots to sample the r-z plane of MRX. A total of 1,700 shots are scrutinized to assemble a refined dataset. We checked for consistency in magnetic-field structure and reference Langmuir probe data in the scrutiny. The X-point location of the reconnection layer had a minor shot-to-shot variation with respect to the system coordinates of MRX. We corrected for the slight change in the X-point location by using the relative positions of the probes measured from the X-point in our GPR analysis.

Fig. 1 demonstrates the effectiveness of GPR in the reconstruction of the density profile and in the prediction of the associated uncertainty. Fig. 1a shows the mean profile of the density extracted from the posterior of the trained GPR model. The 2D density profile shows a pair of high density and low density regions in the vicinity of the separatrices. To validate these features, we compared the mean profile and error bars with the raw data. A visual comparison of a 1-D cut of the mean profile at $\Delta z = 4.5$ cm in Fig. 1b shows that the mean profile follows the trend in the raw data points. The 1-σ confidence interval predicted by GPR is shown by the blue band in Fig. 1b. A visual inspections shows that the width of the 1-σ confidence interval follows the local spread of the raw data points. For example, the error bar is larger at $\Delta r \sim -2.5$ cm where the spread in the raw data is more, while the error bar is smaller at $\Delta r \sim 4.5$ cm where the spread in the raw data is small. Furthermore, we quantitatively checked the 1-σ error bar by comparing the number of raw data points lying within $n_{\text{mean}} \pm 1\sigma$ to those lying outside the error bars. We found 67% of the raw data points to lie within the error bars, which is very close to the theoretical expectation where 68% of the data points are expected to lie within $\pm 1\sigma$ confidence interval. Thus the comparison between raw data and GPR predictions show that GPR is effective at predicting mean profiles and quantifying the uncertainty associated with

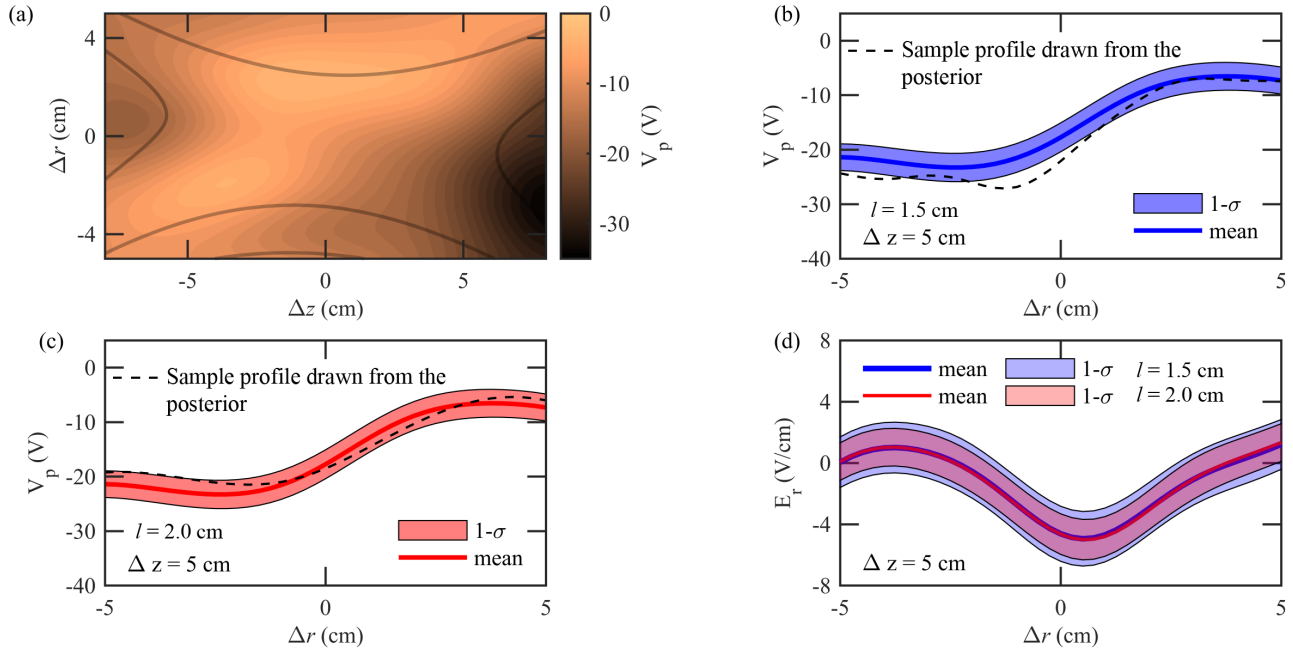

FIG. 2. Demonstration of gradient calculation and determination of the associated error bars using the GPR framework. We also show the effect of the length scale l of the correlation function ρ on the uncertainty in the calculated gradient. The two-dimensional mean profile of plasma potential V_p extracted from the posterior of a GPR model trained using the discrete raw data points is shown in (a). The grey lines in (a) are representative magnetic field lines in the r-z plane for reference. A 1-D plot showing the radial variation of the mean and standard deviation of V_p for $l = 1.5$ and 2 cm are shown in (b) and (c), respectively. Note that the mean and standard deviation in (b) and (c) does not depend on l, which is expected as l does not influence the variance. Rather l affects the smoothness of the sample drawn from the posterior of the trained model. This is because l affects the correlation between spatially separated data points extracted from the posterior. The radial electric field $E_\mathrm{r} = -\partial V_\mathrm{p}/\partial r$ calculated for the two cases $l = 1.5$ and 2 cm is shown in (d). Note that the error bar in the E_r calculation is smaller for the $l = 2$ cm case as the profiles drawn from the posterior are relatively smoother.

those predictions.

B. Calculation of gradient using GPR framework

GPR is useful for computing gradients from data profiles and estimating the associated error bars. For calculating gradients, many sample data profiles were randomly drawn from the posterior of a trained GPR model. Spatial gradients were calculated for each data profile to obtain an ensemble of spatial gradient profiles. The multiple profiles of spatial gradients were averaged to get the mean profile of the data gradient, and the standard deviation was computed to estimate the uncertainty in the gradient calculation.

The magnitude of the error bar of the gradient calculated by the above method depends on the correlation length scale l used for ρ in Eq. 1. We demonstrate the effect of l on uncertainty estimates for gradients using the electric field calculation as an example.

The electric field was calculated from the negative gradient of the plasma potential profiles. The GPR model was trained using diescrete plasma potential data points to extract the plasma potential profiles from the posterior. The discrete data points of the plasma potential were calculated using $V_\mathrm{p} = V_\mathrm{f} + 3.7T_e$ [11]. Here V_p is the plasma potential, V_f is the floating potential, and T_e is the electron temperature. The V_f and T_e were measured using a Langmuir probe.

Fig. 2 shows the calculation of radial electric field, E_r, from V_p using $E_\mathrm{r} = -\partial V_\mathrm{p}/\partial r$. Fig. 2b and c shows the radial variation of V_p used for calculating E_r shown in Fig. 2d. The value of l was held at 1.5 cm in Fig. 2b, while l was 2 cm in Fig. 2c. Note that the mean and the error bar of V_p in Fig. 2b and c are the same as l does not effect the mean and the standard deviation. However, the samples drawn randomly from the posterior of GPR are smoother for the $l = 1.5$ cm compared to $l = 2$ cm as l affects spatial correlation of the posterior samples. The E_r profile for the two cases are shown in Fig. 2c. The mean E_r for the cases are nearly identical, however, the error bars are greater for the $l = 1.5$ cm case compared to $l = 2$ cm.

To estimate a value of l for reconstructing data profiles we compared the gradient of the floating potential directly measured using a radial floating probe array with predictions of GPR for different values of l. The results of direct measurement and GPR prediction were found to best agree for $l = 1.5$ cm. Therefore, we used $l = 1.5$ cm for defining ρ in Eq. 1.

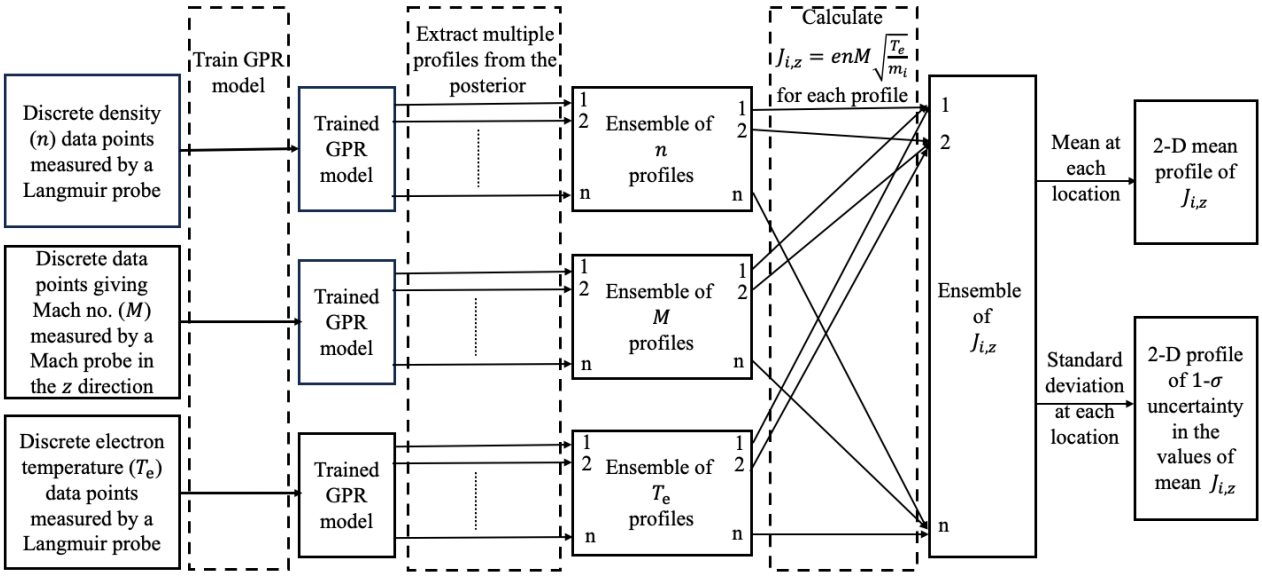

FIG. 3. Schematic of uncertainty propagation in calculation of composite quantities.

C. Error propagation in calculation of composite quantities using a Monte-Carlo method and the GPR framework

GPR provides an effective framework for error propagation in the calculation of composite quantities derived from data profiles of multiple directly measured variables using a Monte-Carlo technique. We use the calculation of the z-component of the ion current density, $J_{i,z} = enM\sqrt{T_e/m_i}$, as an example to demonstrate error propagation. Here, e is the quantum of electric charge, M is the Mach number, T_e is the electron temperature, and m_i is the ion mass. The n and T_e are measured using a Langmuir probe, and M is measured using a Mach probe. The mach probe data was calibrated using ion velocity measured by an ion Doppler spectroscopy probe. The steps of the error propagation calculation are shown in the schematic given in Fig. 3. First, the discrete data points of n, M and T_e are used to train GPR models for each quantity. From the posterior of trained GPR models, many profiles of n, M, and T_e are drawn randomly to calculate $J_{i,z}$ and thus generate an ensemble of $J_{i,z}$ profiles. The multiple profiles of $J_{i,z}$ are averaged to obtain the mean profile of $J_{i,z}$, and the standard deviation gives the uncertainty.

III. DISCUSSION

In this supplementary material, we have described the use of GPR to reconstruct 2D data planes and compute gradients of physical quantities (n, T_e, V_p, Mach number, etc.) from datasets of discrete data points obtained by electric probes. The electric probes were used to make single-point measurements in each shot, and the probes were moved in between shots to cover the r-z plane of MRX. Single point measurements from a large number of shots were assimilated to form a dataset of discrete data points for the application of GPR. The 2D reconstructed data planes of the electric probe data, along with the magnetic field data of the 2D B-dot probe array, are used for physics analysis of the reconnection layer. The error propagation in the calculation of composite quantities was done using a Monte-Carlo method.

[1] C. E. Rasmussen, *Gaussian processes for machine learning*, Adaptive Computation and Machine Learning series (MIT Press,, Cambridge, Mass. :, 2005-01-01).

[2] M. Chilenski, M. Greenwald, Y. Marzouk, N. Howard, A. White, J. Rice, and J. Walk, Nuclear Fusion **55**, 023012 (2015).

[3] A. Mathews and J. W. Hughes, IEEE Transactions on Plasma Science **49**, 3841 (2021).

[4] J. Wang, arXiv preprint arXiv:2009.10862 (2020).

[5] Q.-H. Zhang and Y.-Q. Ni, IEEE Transactions on Signal Processing **68**, 3450 (2020).

[6] M. Yamada, H. Ji, S. Hsu, T. Carter, R. Kulsrud, N. Bretz, F. Jobes, Y. Ono, and F. Perkins, Physics of

Plasmas **4**, 1936 (1997).
[7] M. Chilenski, M. Greenwald, A. Hubbard, J. Hughes, J. Lee, Y. Marzouk, J. Rice, and A. White, Nuclear Fusion **57**, 126013 (2017).
[8] J. Yoo, *Experimental studies of particle acceleration and heating during magnetic reconnection*, Ph.D. thesis, Princeton University (2013).
[9] F. Pedregosa, G. Varoquaux, A. Gramfort, V. Michel, B. Thirion, O. Grisel, M. Blondel, P. Prettenhofer, R. Weiss, V. Dubourg, J. Vanderplas, A. Passos, D. Cournapeau, M. Brucher, M. Perrot, and E. Duchesnay, Journal of Machine Learning Research **12**, 2825 (2011).
[10] Gaussian processes, https://scikit-learn.org/stable/modules/gaussian_process.html, [Online; accessed 5-July-2023].
[11] H. Ji, H. Toyama, K. Yamagishi, S. Shinohara, A. Fujisawa, and K. Miyamoto, Review of Scientific Instruments **62**, 2326 (1991).